

Article

Stress-Dependent Permeability of Fractures in Tight Reservoirs

Nai Cao ¹, Gang Lei ^{2,*} , Pingchuan Dong ^{1,*} , Hong Li ¹, Zisen Wu ^{1,3} and Yudan Li ¹

¹ College of Petroleum Engineering, China University of Petroleum Beijing, Beijing 102249, China; caonai99@163.com (N.C.); lihong660@163.com (H.L.); 1533141753@ku.edu (Y.L.)

² College Petroleum of Engineering & Geoscience, King Fahd University of Petroleum and Minerals, Dhahran 31261, Saudi Arabia; gang.lei@kfupm.edu.sa

³ Beijing Technical Market Management Office, Beijing 100032, China; wuzisen@163.com

* Correspondence: gang.lei@kfupm.edu.sa (G.L.); dpcfem@163.com (P.D.); Tel.: +86-186-0120-0950 (P.D.)

Received: 4 December 2018; Accepted: 29 December 2018; Published: 29 December 2018



Abstract: Permeability is one of the key factors involved in the optimization of oil and gas production in fractured porous media. Understanding the loss in permeability influenced by the fracture system due to the increasing effective stress aids to improve recovery in tight reservoirs. Specifically, the impacts on permeability loss caused by different fracture parameters are not yet clearly understood. The principal aim of this paper is to develop a reasonable and meaningful quantitative model that manifests the controls on the permeability of fracture systems with different extents of fracture penetration. The stress-dependent permeability of a fracture system was studied through physical tests and numerical simulation with the finite element method (FEM). In addition, to extend capability beyond the existing model, a theoretical stress-dependent permeability model is proposed with fracture penetration extent as an influencing factor. The results presented include (1) a friendly agreement between the predicted permeability reduction under different stress conditions and the practical experimental data; (2) rock permeability of cores with fractures first reduces dramatically due to the closure of the fractures, then the permeability decreases gradually with the increase in effective stress; and (3) fracture penetration extent is one of the main factors in permeability stress sensitivity. The sensitivity is more influenced by fracture systems with a larger fracture penetration extent, whereas matrix compaction is the leading influencing factor in permeability stress sensitivity for fracture systems with smaller fracture penetration extents.

Keywords: fractured tight reservoir; stress-dependent permeability; fracture penetration extent; theoretical model

1. Introduction

Fluid flow under stress through fractured media has drawn considerable attention in many engineering fields, including physics [1,2], hydraulics [3,4], chemistry [5], petroleum, and engineering [6–10]. The permeability of a reservoir decreases as effective stress increases during reservoir development [11]. This permeability reduction is more severe for fractured reservoirs, which poses difficulties for oil production in tight reservoirs due to seepage losses [12]. Since permeability is one of the key factors in reservoir production, understanding the mechanism of permeability reduction assists with reservoir dynamic analysis and production optimization.

Many studies have been conducted on the law of reservoir stress sensitivity, with many of them focused on experimentation. Buchsteiner et al. [13] found that the closure of fractures occurs due to rock pore structure deformation under increasing stress. The permeability damage rate under changing stress was defined in the explanation of the stress sensitivity of low permeability gas formation [14].

Stress sensitivity experiments have been conducted under a wide range of stresses [15], and variation patterns have been directly measured [16]. Fractured reservoirs, in the low permeability stage, were found to have greater stress sensitivity, which is weakened when the effective stress is higher beyond a certain criteria [17]. Besides the above experimental works, theoretical works requiring complicated study methods [18] and microimage analysis systems [19] have also been conducted. The physical structure model of the fracture surface [20] and the mechanical structure model of the surface contact of fractures [21] have been established. The change between fracture volume loss and effective stress was determined [22–24]. McKee et al. [25] derived a function for porosity considering effective stress, and substituted the equation for porosity into the Carman–Kozeny equation to calculate the permeability of fractures considering the fracture aperture and fracture height. However, not much attention has been paid to the impact caused by the extent of fracture penetration on stress-dependent permeability, and the fracture has rarely been separated as a distinct object. We still do not fully understand the characteristic behavior of the stress-dependent permeability of a fractured reservoir or the effects of fracture parameters [26].

Numerical methods are effective at simulating the flow behavior in fractured porous media [27–30]. A two-dimensional (2D) fracture model proposed by Perkins and Kern and developed by Nordren (the PKN model) [27], which assumes that fractures have an elliptical cross-section and constant height, has been used to simulate the settling velocity correlation of proppant in foam fracturing. A full three-dimensional (3D) displacement discontinuity method (DDM) has been used to investigate proppant transportation in growing fracture networks [28]. A hybrid Eulerian–Lagrangian model, assuming that foam is a single-phase non-Newtonian fluid, has been used to conduct the simulation of media with hydraulic fractures [29]. A hydraulic fracturing simulator that implicitly couples fluid flow with 3D discrete fracture networks (DFNs) has been established [30]. Due to the advantage of better precision and higher computational efficiency to simulate coupled flow deformation behavior in porous media, FEM simulation was adopted in this work to simulate the stress-dependent permeability change in tight media with fractures.

The major goal of this work is to take the fracture system as a distinct object and explore the impact on stress-dependent permeability caused by a fracture system with different fracture parameters. The specific objectives are to (1) analyze the stress-dependent permeability variation in the fracture system caused by the extent of the fracture penetration, (2) develop a reasonable model to quantify the stress-dependent permeability loss of the fracture system, (3) compare the predicted results with experimental results to support the model results, and (4) to quantitatively determine the influences of different fracture penetration extents on permeability in fractured porous media. A technology roadmap of this work is presented in Figure 1.

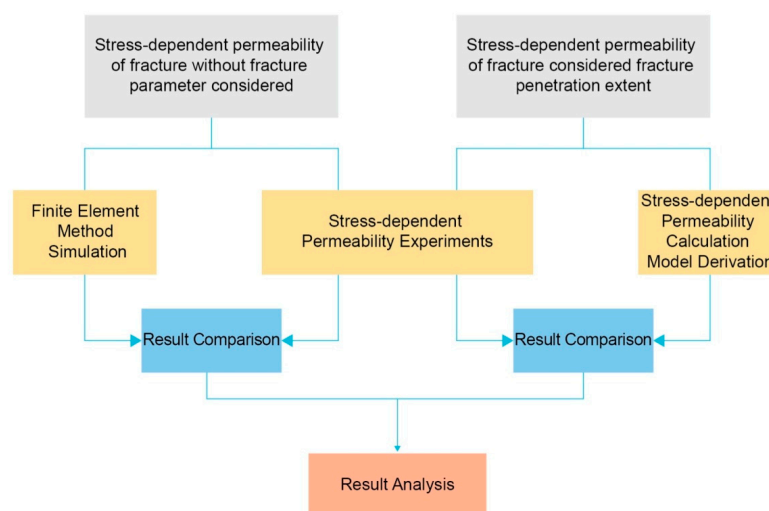


Figure 1. The technology roadmap of the work.

2. Experiment

2.1. Samples

The preparation of samples involved core drilling, eluting, drying, and fracture forming. Cores, 2.5 cm in diameter and 15 cm in length, were drilled along the horizontal direction of full-size core samples from a tight sandstone reservoir. The elution of drilled cores was conducted in an extractor with different solutions. They were first eluted using benzene, and then by a mixed solution of alcohol and toluene at a ratio of 1:3. After the elution, the cores were placed in a vacuum drying oven, vacuumed and dried to a constant weight for 24 h at a temperature range of 60–65 °C, with a relative humidity of 40% to 45%, and then moved to a dryer to cool down to room temperature.

Since the drilled cores potentially had tiny distributed fractures, confining pressure was applied to close those fractures in order to better control the variation. The fractures with different penetration extents in the cores were formed through different methods. For a fully penetrated core, the Brazilian split technique [31,32] was adopted. For the cores with different penetration extents, a specific control method was needed to set the fracture [33]. Alloy structure steel wires were used to form a concentrated stress in order to induce a radial tension crack. As shown in Figure 2, a pressure p (MPa) was exerted on the steel wires and a fracture formed along the direction of the exerted pressure. The extent of the fractures was controlled by monitoring the differential stress.

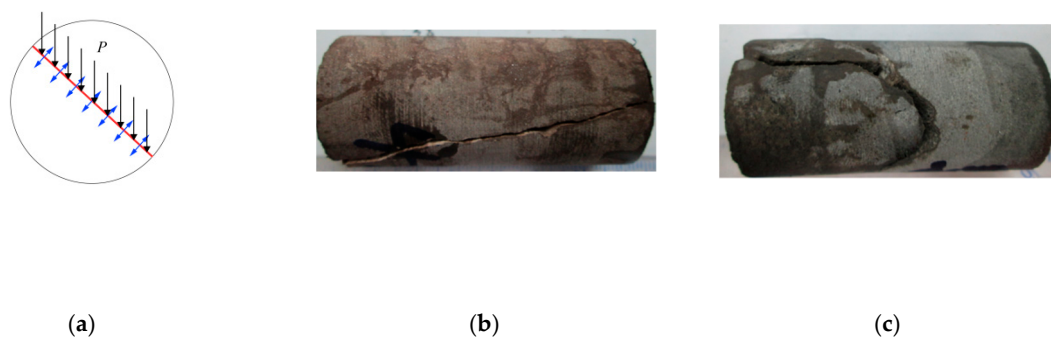


Figure 2. (a) A sketch of the fracture-forming method in cores with different penetration extents. The red line is the alloy structure steel wire, the pressure represented by the black arrows is exerted directly on the wire in the normal direction of the upper plate of the core, and the crack occurs along the direction of the blue arrows. (b) A fully penetrated core and (c) partly penetrated core.

In the stress sensitivity experiments on the matrix and fractured cores, the porosity and permeability were measured in the laboratory (Table 1). Three sets of tight cores with different permeability levels were selected, and each set contained 2 matrixes with the same permeability level. Fractures were formed using the Brazilian split technique [34,35] in one of the two cores in each set, with the fracture surface remaining uncontaminated. The parameters of the cores are summarized in Table 1.

Table 1. Physical parameters of the matrix and fractured cores.

No.	Core Type	Core Diameter (cm)	Core Length (cm)	Width of Fracture (cm)	Porosity (%)	Permeability ($10^{-3} \mu\text{m}^2$)
1	Matrix	2.46	7.24	0.00	14.7	0.52
	Fractured core	2.46	7.24	2.41	14.7	1.08
2	Matrix	2.53	6.37	0.00	15.2	0.72
	Fractured core	2.53	6.37	2.42	15.2	1.27
3	Matrix	2.48	8.35	0.00	15.4	0.90
	Fractured core	2.48	8.35	2.44	15.4	1.43

In the experiment, the permeability stress sensitivity experiments were conducted on tight cores with five different fracture penetration extents including a matrix without fractures and those with 25, 50, 75, and 100% penetration of the core. The parameters are shown in Table 2.

Table 2. Physical parameters of the cores with different penetration extents.

Core Type	Core Diameter (cm)	Core Length (cm)	Width of Fracture (cm)	Permeability ($10^{-3} \mu\text{m}^2$)	Permeability Increase Multiple
Matrix	24.62	31.30	0.00	0.052	1.00
Fracture penetration 25%	24.62	31.30	24.16	0.058	1.12
Fracture penetration 50%	24.62	31.30	24.16	0.065	1.25
Fracture penetration 75%	24.62	31.30	24.16	0.074	1.42
Fracture penetration 100%	24.62	31.30	24.16	0.086	1.65

2.2. Experimental Apparatus

The schematic of the apparatus used for the stress-dependent permeability experiment is shown in Figure 3. The driving pressure was provided by a high-pressure injection pump, equipped with a high-pressure container. The recording range of the flow rate of this pumping was between $0.01 \mu\text{L}/\text{min}$ and $50 \text{ mL}/\text{min}$, with an accuracy of $0.01 \mu\text{L}/\text{min}$. Its pressure ranged from 0.068 MPa to 68 MPa , with an accuracy of 7 kPa . A hand pump was connected to the cylindrical core holder to provide confining pressure. The inlet and outlet pressure difference was recorded by a differential pressure transducer.

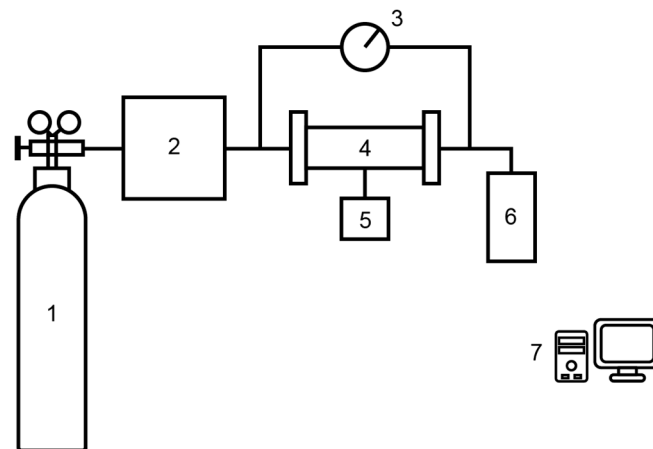


Figure 3. Schematic of the apparatus used for the stress-dependent permeability experiment: 1, High-pressure gas source; 2, Pressure control panel; 3, Pressure sensor; 4, Core holder; 5, Hand pump; 6, Measuring cylinder; and 7, Data acquisition system.

2.3. Experimental Procedure

Determining the relationship between effective stress and permeability is the key objective of stress sensitivity experiments. In this work, stress sensitivity experiments were conducted under variable confining pressure in an unsteady state, and the gas used here was N₂. Primary effective stress was used to evaluate stress sensitivity of the tight core [25,34,35]:

$$\sigma = \sigma_0 - \eta p \quad (1)$$

where σ is the primary effective stress (MPa), σ_0 is the confining pressure (MPa), p is the fluid pressure (MPa), and η is the effective stress coefficient, which can be taken as rock porosity of the matrix system and the unity of the fracture system.

The porosity of the experimental core was obtained using the gas pore volume measurement method. (1) Place the standard sample in the standard chamber under a pressure P_1 , (2) place the core in the rock chamber, (3) connect the two chambers until the pressure stabilizes at P_2 , and (4) calculate the core porosity by the volume and pressure [36]. The primary permeability experiment can be summarized as follows: (1) put the sample into the core holder, and maintain it under a constant pressure drop; (2) apply confining pressure and gradually increase it to 30 MPa in 5 MPa increments. After the gas flow is stable, record the pressure at the core outlet and inlet and the flow rate of outlet. (3) Calculate the permeability and permeability loss ratio based on the records.

3. Numerical Simulation

3.1. Finite Element Method

Based on computed tomography (CT) scanned images of the tested cores, the pores and the skeleton of the porous media were classified, and then the permeability of the porous media was determined using the FEM using ANSYS software (ANSYS, Inc., Pittsburgh, PA, US) [37–41].

The stress-dependent permeability of the porous media was simulated using a two-way Fluid Structure Interaction (FSI) approach involving both Computational Fluid Dynamics (CFD) and structural mechanics analysis. The pressure/loads of the single-phase water flow in porous media were calculated using ANSYS. The FEM calculation steps with ANSYS software can be divided into three basic steps: mesh division, unit analysis, and overall analysis [42,43]. The mesh division of the matrix and fractured cores are presented in Figure 4a,b, respectively, in which the matrix is presented by grey and the fracture and cores are represented by brown. Along with the ANSYS software, TetraMesh (mesh division method with tetrahedron as mesh unit) was used. The size of the core was $200 \times 200 \times 200$ pixels, with a pixel size of $0.4 \mu\text{m}$, porosity 11.24%, with 24,3520 matrix elements, and 336,224 pore and fracture elements. After the fluid pressure on the fluid–solid interface was transferred to the ANSYS structural solver, the meshes on the fluid–solid interface of both the rock matrix and pore model were remeshed according to the deformation data.

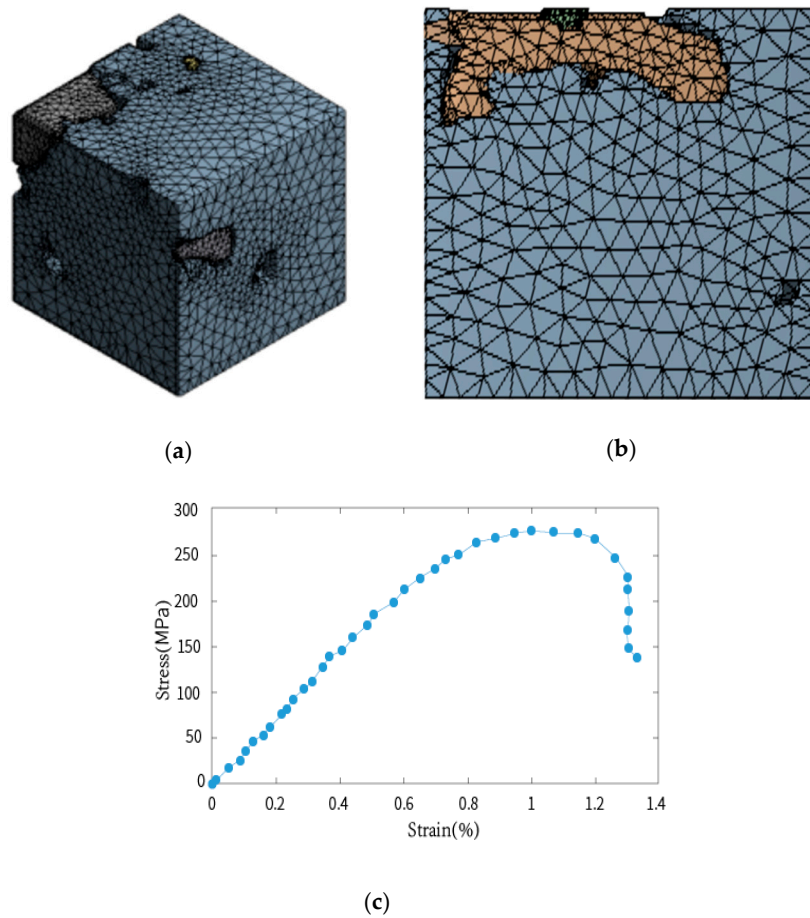


Figure 4. The mesh division and stress–strain curve of the simulation of tested cores: (a) mesh division of the core without fractures, (b) mesh division for the core with fractures, and (c) stress–strain curve.

The specific input and assumptions were required in order to use FEM in engineering materials [44–46]. The simulation is based on the assumption that fluid is incompressible, the density is constant, and the flow is laminar. Since the fracture width was much larger than the fracture opening, the flow in the fracture was simplified as a two-dimensional flow. To present the differences in the fractures and the matrix, different physical material properties were adopted. The pores and fractures were filled with units, the skeleton was built as nonlinear elastic material, and the input model material parameters shown in Table 3 were set based on the FEM work conducted by Zheng [47], which were close to those of natural sandstone and artificial sandstone. The stress–strain curve of the tested cores, which was used as the material property for the structural analysis in the simulation, is shown in Figure 4c.

Table 3. The main input parameters for FEM simulation.

Calculation Unit	Elastic Modulus (GPa)	Poisson's Ratio	Internal Friction Angle (°)	Cohesion Force (MPa)
Matrix	35.6	0.2	15	20
Fracture and Pores	3.56	0.3	20	2

In the simulation, fixed constraints were applied to the upper and lower boundaries of the model, the other two sides were loaded with lateral pressure to simulate confining pressure in the stress sensitivity experiment, and the lateral pressure was gradually increased to 30 MPa in 5 MPa increments. The boundary conditions of the matrix model and pore model were set separately in

the ANSYS workbench. The contact surfaces of solid and fluid inside the rock were defined as the fluid–solid interface through which pressure is transmitted between the solid and fluid. The geometric nonlinearity of the system elements was considered. At the end of each load step, the system searched for the approximate balanced configuration of the system structure according to the displacement of the node, considering the change in the stiffness of the model structure, and calculated the model flexibility matrix. The permeability of the porous media under stress conditions can be determined by combining the Navier–Stokes and stress equations. All simulations converged after different numbers of iterations under the condition that the absolute convergence criteria was set to 10^{-5} for all equations, for which default relaxation factors were used.

3.2. Stress-Dependent Permeability Model

Primary effective stress was chosen to evaluate the stress sensitivity of the tight core, which is described as [41]:

$$K = K_0 e^{-\alpha(\sigma_0 - \eta p)} \quad (2)$$

where K_0 is the initial permeability of the rock ($10^{-3} \mu\text{m}^2$), K is the rock permeability under stress ($10^{-3} \mu\text{m}^2$), α is the permeability stress sensitivity coefficient (MPa^{-1}), σ_0 is the overlying rock stress (MPa), p is fluid pressure (MPa), and η is the effective stress coefficient, which can be taken as the rock porosity in the matrix system and 1 in the fracture system [34,35].

Under the assumption that seepage of gas is steady in fractured cores and based on Darcy's equation, the permeability of the matrix system can be described as:

$$K_m = -\frac{Q_m p_0 \mu}{(A - \omega_f l) p} \frac{dx}{dp} \quad (3)$$

where K_m is the matrix system permeability ($10^{-3} \mu\text{m}^2$), Q_m is the gas flow volume of the matrix system under atmospheric pressure (cm^3/s), p_0 is the atmospheric pressure (MPa), A is the core section area (cm^2), μ is the gas viscosity ($\text{mPa}\cdot\text{s}$), l is the width of the fracture (cm), and ω_f is the fracture opening (cm).

A fracture does not always fully penetrate the reservoir, so the fracture penetration extent is the factor discussed here. We assumed fluid seepage only occurs in the horizontal direction. In the equivalent resistance method, the equivalent length of the oblique fracture length can be taken as its projection in the horizontal direction. Therefore, the direction of the fracture can be equated as the horizontal direction, as shown in Figure 5.

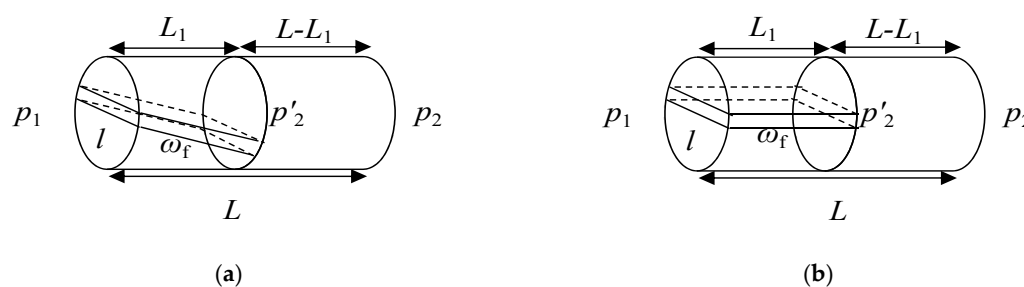


Figure 5. The sketch of a fracture-penetrated core (a) with an oblique fracture and (b) after an equivalent fracture is made. l is the width of the fracture (equal to the diameter of the section surface) (cm); ω_f is the fracture opening equal to the distance of the two surfaces of the fracture (cm); L_1 is the equivalent length of the fracture (cm); L is core length (cm); p_1 is the absolute pressure on the inlet section (MPa); p_2 is the absolute pressure on the outlet section (MPa); p'_2 is the absolute pressure on the outlet section of the penetrated part (MPa); and the fracture penetration extent is L_1/L .

The gas flow volume through the matrix of the penetrated part is:

$$Q_m = \frac{(A - \omega_{f0}l)(p_1^2 - p_2'^2)K_{m0}}{2\mu p_0 L_1} \quad (4)$$

where Q_m is the gas flow volume through the matrix of the penetrated part (cm^3/s), K_{m0} is the initial core matrix permeability ($10^{-3} \mu\text{m}^2$), p_1 is the absolute pressure on the inlet section (MPa), p_2' is the absolute pressure on the outlet section of the penetrated part (MPa), L_1 is the equivalent length of the fracture (cm), and ω_{f0} is the fracture system opening before stress is exerted (cm).

The gas flow volume through the fracture system is calculated as:

$$Q_f = \frac{\omega_{f0}l(p_1^2 - p_2'^2)K_{f0}}{2\mu p_0 L_1} \quad (5)$$

The gas flow volume through the part without a fracture is calculated as:

$$Q_{s1} = \frac{A(p_2'^2 - p_2^2)K_{m0}}{2\mu p_0(L - L_1)} \quad (6)$$

The total gas flow volume through the core is:

$$Q_{s2} = \frac{A(p_1^2 - p_2^2)K_{s0}}{2\mu p_0 L} \quad (7)$$

where Q_f is the gas flow volume through the fracture system under atmospheric pressure (cm^3/s), Q_{s1} is the gas flow volume through the part without a fracture under atmospheric pressure (cm^3/s), Q_{s2} is the total gas flow volume through the fractured core under atmospheric pressure (cm^3/s), p_2 is the absolute pressure on the outlet section (MPa), L is the core length (cm), K_{s0} is the initial total permeability of the fractured core ($10^{-3} \mu\text{m}^2$), and K_{f0} is the initial fracture permeability ($10^{-3} \mu\text{m}^2$).

Considering the continuity of the fluid, the gas flow volume through the part without fractures should be equal to the total gas flow volume that flows through the fractured part of the core, which is the sum of the gas flow volume through the fracture system and the matrix. The following equations are obtained:

$$p_2'^2 = p_2^2 + \frac{L - L_1}{L} \frac{K_{s0}}{K_{m0}} (p_1^2 - p_2^2) \quad (8)$$

$$AK_{s0} = \frac{K_{m0}L - K_{s0}(L - L_1)}{K_{m0}L_1} [(A - \omega_{f0}l)K_{m0} + \omega_{f0}lK_{f0}] \quad (9)$$

Based on cube law, the relationship between the fracture opening and fracture permeability satisfies:

$$K_{f0} = \frac{\omega_{f0}^2}{12} \quad (10)$$

Then, the following equation can be derived, based on which initial fracture opening and the initial permeability K_{f0} of the fracture system:

$$\omega_{f0}^3 - 12K_{m0}\omega_{f0} + \frac{12AK_{m0}}{l} - \frac{12AK_{s0}}{l} \frac{K_{m0}L_1}{K_{m0}L - K_{s0}(L - L_1)} = 0 \quad (11)$$

With the confining pressure σ_0 , the inlet pressure p_1 , and the outlet pressure p_2 on the sample, the effective stress (MPa) exerted on the core is:

$$\sigma = \sigma_0 - \eta \left(\frac{p_1 + p_2}{2} \right) \quad (12)$$

The gas flow volume through the matrix of the penetrated part under effective stress is:

$$Q_m = \frac{K_{m0}e^{-\alpha_m\sigma}}{2p_0\mu L_1} \left(A - 2\sqrt{3}K_f^{\frac{1}{2}}l \right) (p_1^2 - p_2'^2) \quad (13)$$

The gas flow volume through the fracture system and the part without a fracture are, respectively:

$$Q_f = \frac{2\sqrt{3}(p_1^2 - p_2'^2)l}{2p_0\mu L_1} K_f^{\frac{3}{2}} \quad (14)$$

$$Q_{s1} = \frac{A(p_2'^2 - p_2^2)K_{m0}e^{-\alpha_m\sigma}}{2\mu p_0(L - L_1)} \quad (15)$$

The total gas flow volume through the core is calculated as:

$$Q_{s2} = \frac{A(p_1^2 - p_2^2)K_{s0}e^{-\alpha_s\sigma}}{2\mu p_0 L} \quad (16)$$

where α_m is the matrix permeability stress sensitivity coefficient (MPa^{-1}), α_s is the permeability stress sensitivity coefficient of the fractured core (MPa^{-1}), and K_f is the fracture permeability after stress is exerted ($10^{-3} \mu\text{m}^2$).

Based on the continuity, the following equations are obtained:

$$p_2'^2 = p_2^2 + \frac{L - L_1}{L} \frac{K_{s0}e^{-\alpha_s\sigma}}{K_{m0}e^{-\alpha_m\sigma}} (p_1^2 - p_2^2) \quad (17)$$

$$K_f^{\frac{3}{2}} - K_{m0}e^{-\alpha_m\sigma}K_f^{\frac{1}{2}} - \frac{\sqrt{3}A}{6l} \left(\frac{K_{s0}e^{-\alpha_s\sigma}K_{m0}e^{-\alpha_m\sigma}L_1}{K_{m0}e^{-\alpha_m\sigma}L - K_{s0}e^{-\alpha_s\sigma}(L - L_1)} - K_{m0}e^{-\alpha_m\sigma} \right) = 0 \quad (18)$$

Based on the equations above, the permeability loss ratio of the fracture system γ (%) can be determined as:

$$\gamma = \frac{K_f}{K_{f0}} \quad (19)$$

4. Results and Discussion

4.1. Experimental Results

4.1.1. Matrix and Fractured Cores

Stress sensitivity experiments under different effective stresses were conducted on all cores according to the Standard SY/T6385—2016 [48], and the permeability stress sensitivity curves are shown in Figure 6a–c. The permeability of matrix and fractured cores was damaged to some degree due to the effective stress increase. Compared with the fractured cores, the permeability stress sensitivity of the matrix was weaker, and the damage range of permeability was relatively smaller. Rock compaction is the dominant factor in the stress-dependent permeability of the matrix. The permeability variation trends are almost linear when compared with those of the fractured cores. A possible reason for this is that the stress-dependent permeability of the matrix is purely determined by rock compaction, whereas those of cores with fractures are a combination of rock compaction and fracture closure. Then, for the fractured cores, a larger damage range and faster permeability rate of decrease were observed. The rate of decrease slows down when the permeability of the fractured cores decreases to a point equal to that of the matrix. The stress-dependent permeability could be divided into two stages. In the first stage, fracture closure is the leading factor with the rock compaction working together; in the second stage, the rock compaction is the dominant factor.

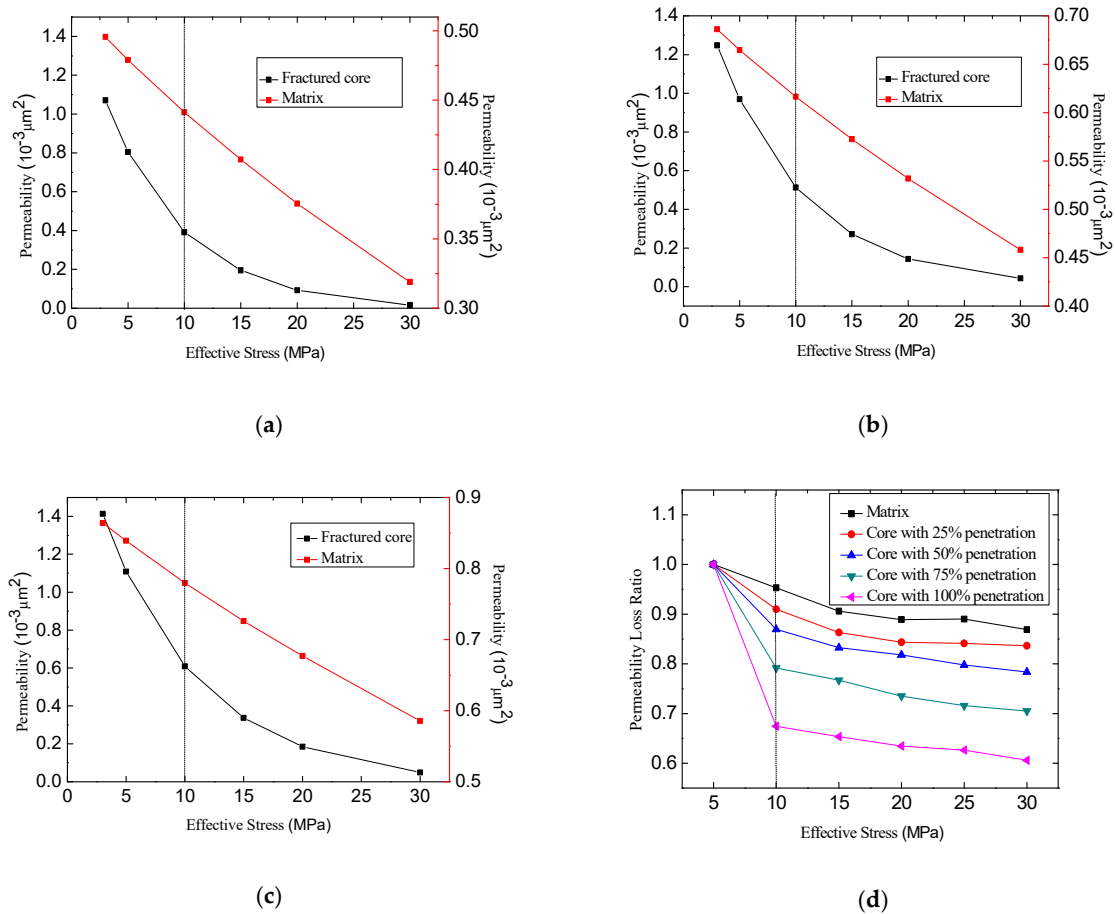


Figure 6. The experimental results of stress-dependent permeability of cores in (a) set 1, (b) set 2, and (c) set 3, and (d) fractured cores with different penetration extents.

4.1.2. Fractured Cores with Different Fracture Penetration Extents

The permeability stress sensitivity curve shown in Figure 6d suggests that permeability loss occurred in all tested cores, and stress sensitivity increased with the increasing fracture penetration extent. The permeability stress sensitivity curves for the fractured cores were similar to that for the matrix when the penetration extent was small, suggesting that permeability is mainly dominated by the matrix in this case. The rock stress response process can be divided into the fracture closure stage and the rock compaction stage, with a larger extent of fracture penetration. During the first stage, rock permeability dramatically reduces due to the closure of the fractures, and in the second stage, the permeability decreases slowly with the increase in the effective stress due to matrix compaction.

4.2. FEM Simulation Results

To verify the FEM simulation, the measured permeability and effective stress were compared with the predicted values from FEM simulation (Figure 7). A definitive negative correlation between the permeability and effective stress is demonstrated in Figure 7. As for the matrix (Figure 7a), the permeability decreased at a relatively constant rate, whereas the permeability of the fractured core (Figure 7b) first dramatically decreased and then slowed down with increasing effective stress. The results (Figure 7) suggest that the simulated changing trend of the stress-dependent permeability is the same as that of the experimental results. However, the permeability predicted from FEM simulation is larger than measured during the experiment under a given effective stress. The main reason for this is that the effective resolution of CT is limited by the voxel size: many narrow pores with smaller pore radii cannot be easily detected, and only a limited range of pore throat radii can be detected. Therefore,

the permeability predicted by FEM simulation is larger than the experimental findings under a given effective stress.

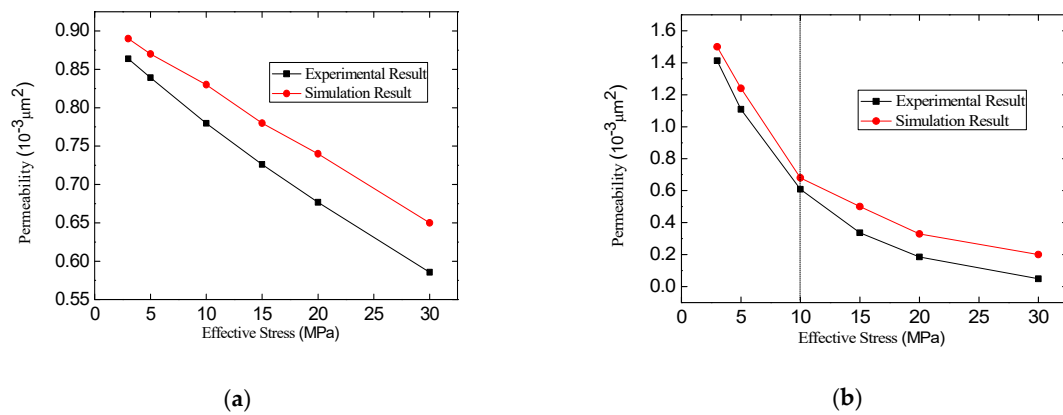


Figure 7. Simulation and experimental results of stress-dependent permeability: (a) matrix and (b) fractured core.

4.3. Comparison of Model and Experimental Results

To evaluate the performance of the proposed model, Equation (19) and experimental data were used for comparison. Based on the parameters summarized in Tables 1 and 2, the permeability loss ratio was measured, calculated, and plotted (Figure 8). The results suggest that this calculation model can fairly accurately predict the permeability loss ratio; the average relative errors between the measured and predicted results were all within 2.5%.

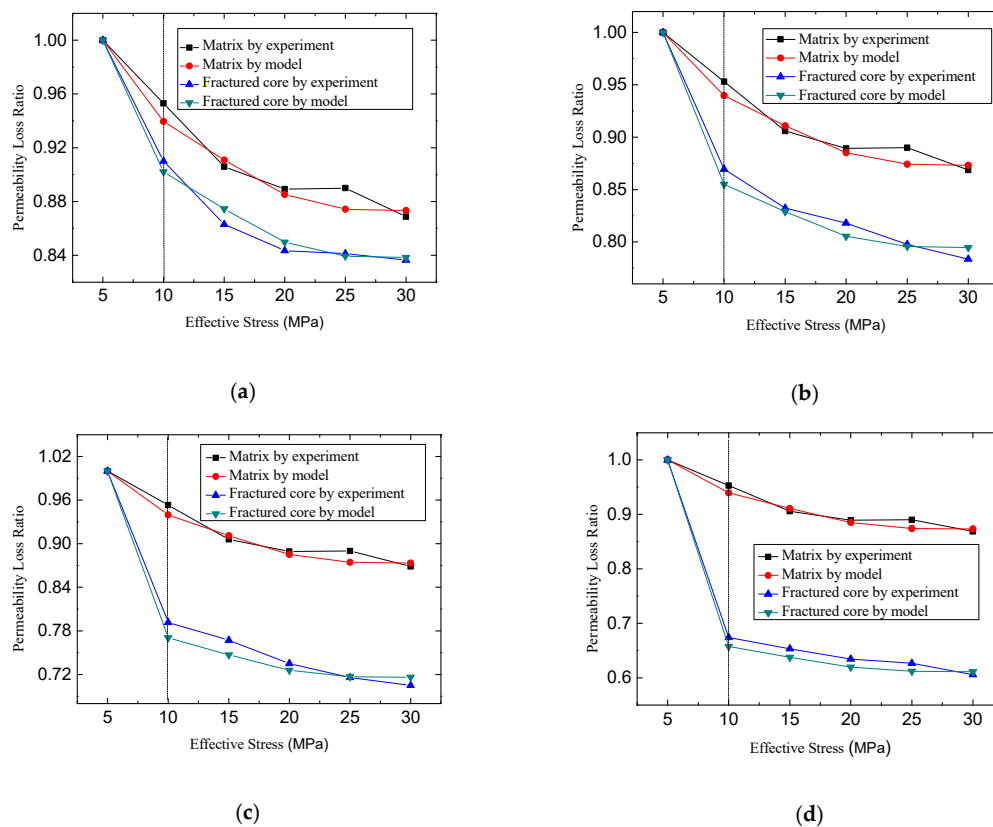


Figure 8. Comparison curve for the experimental data and model results. Core with (a) 25%, (b) 50%, (c) 75%, and (d) 100% penetration.

4.4. Influencing Factor Analysis

4.4.1. Fracture Penetration Extent

The resulting permeability loss ratio variation versus effective stress under different fracture penetration extents is shown in Figure 9a. The result illustrates that the permeability of the fracture quickly decreased before reaching 10 MPa and then smoothed (Figure 9a). This suggests that the deformation process of the fractured cores can be divided into two stages: the fracture closure stage and matrix compaction stage. In the first stage, with a lower effective stress, the permeability of the fractured cores quickly decreases. When the effective stress increases to 10 MPa (stage 2), the fracture system closes, and the matrix system is compressed. The permeability stress sensitivity has a positive relationship with the penetration extent, as shown in Figure 9a. The permeability loss ratio increases with increasing fracture penetration extent. The permeability loss ratios of the cores with different fracture penetration extents are compared in Figure 9b–e. This suggests that, under the same effective stress, the fracture has the highest stress sensitivity, followed by the fractured cores, and the matrix has the lowest stress sensitivity of the three. These figures demonstrate that the permeability loss ratio increases with increasing fracture penetration extent. With an increasing penetration extent, the permeability sensitivity curve shows a trend approaching that of the fracture. Thus, during the production process, a reasonable pressure drop and effective stress should be determined according to the fracture penetration extent in order to preclude damage to the permeability of the reservoir due to stress sensitivity.

4.4.2. Permeability Increasing Multiples

The change in the deviation extent versus the increasing multiples of the initial permeability of the fractured core is shown in Figure 9f. This shows that with increasing permeability multiples (i.e., the ratio of fractured core permeability to permeability of matrix core), the deviation extent of the permeability loss ratio of the fractured core to the fracture decreases, whereas that of the fractured core to the matrix system increases. The permeability sensitivity is more heavily influenced by the fracture system with a larger penetration extent and increasing multiples of the initial permeability, and the permeability stress sensitivity curve approaches that of the fracture system, as shown in Figure 9f.

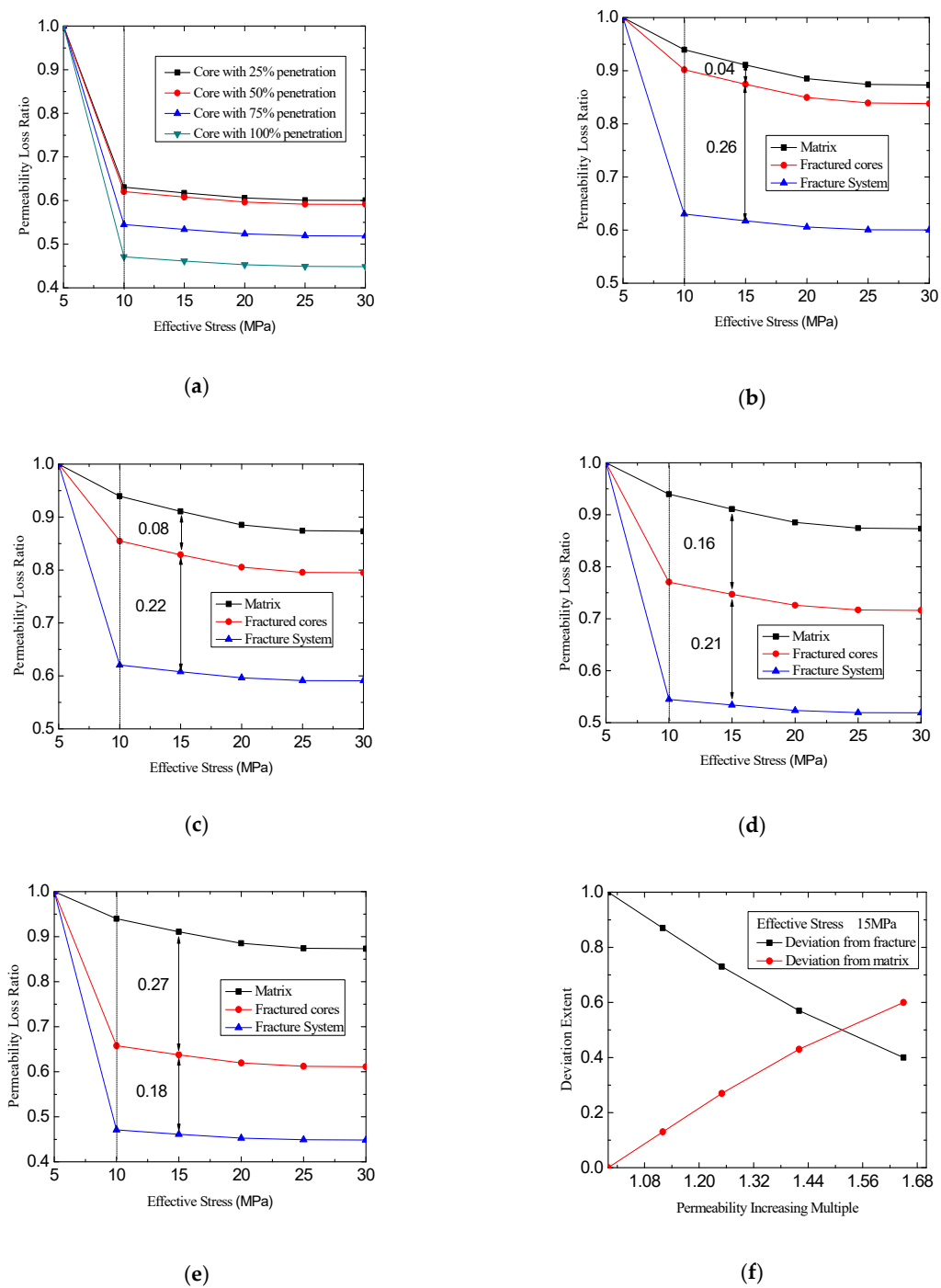


Figure 9. Sensitivity analysis results. Permeability loss ratio curves for (a) cores with different penetration extents, (b) the core with 25% penetration, (c) the core with 50% penetration, (d) the core with 75% penetration, and (e) the core with 100% penetration, and (f) variation curve of the deviation extent and increasing multiples.

5. Conclusions

Through FEM simulation and experiments conducted on the stress-dependent permeability of fractures in cores, we proposed a novel theoretical model for the determination of stress-dependent permeability in tight fractured reservoirs. The model allowed us to analyze the influences caused by a fracture system with different fracture parameters on the stress-dependent permeability reduction in tight fractured reservoirs. Predictions produced by the model presented similar variation trends to

the experimental results. The feature of this model is that every parameter in the model has a specific physical significance, while it lacks empirical constants. The novelty of this work is that the fracture penetration extent is newly introduced as an influencing factor and the fracture system is separated as a distinct objective to be analyzed. We drew the following conclusions:

The deformation of fractured cores can be divided into two stages: the fracture closure stage and the matrix compression stage. During the first stage, rock permeability is dramatically reduced due to the closure of the fracture; in the second stage, the permeability decreases slowly with the increase in the effective stress that continues to compress the rocks. The calculation model, considering the fractured penetration extent, can predict the permeability loss of the matrix, fractured core, and fracture system fairly accurately at pressures up to 20 MPa.

Permeability stress sensitivity is more strongly influenced by the fracture system with a larger penetration extent. In the systems with lesser penetration extent, the matrix compression is the leading factor influencing permeability stress sensitivity.

The stress sensitivity experiments and our corresponding model, considering the fracture penetration extent, could be applied to more accurately predict the production of fractured reservoirs and the coupled flow deformation behavior in fractured porous media, including tight carbonates, tight sandstone, and shale rock. Considering the fracture parameters in the production model or seepage model is crucial. As the extent of the fracture penetration directly affects the reservoir permeability and the mechanism of seepage flow, considering the fracture penetration extent in the proposed stress-dependent permeability model makes our work relevant in product development in tight reservoirs. However, it should be noted that the proposed model ignores the crossflow of fractures, and the stress-dependent permeability could be influenced by the composition, microstructures, mineral disintegration interpretation, mechanical properties, and community of reservoirs. The fluid flow in porous media with fracture systems under effective stress is an interesting and challenging topic, and this work is currently underway.

Author Contributions: This work is completed by all of the authors: N.C. and G.L. produced the main contribution, proposed the main ideas employed in the research, and wrote the original paper; P.D. offered meaningful suggestions and helped to improve the work; Z.W. conducted the visualization of the results; and H.L. and Y.L. provided assistance in the process of this research.

Acknowledgments: The authors are grateful for the financial support from the National Science and Technology Major Projects of China (Grant No.2016ZX05037-003; Grant No.2017ZX05049-003). Special thanks to Y.L. for her support and encouragement in the whole process.

Conflicts of Interest: The authors declare no conflict of interest.

References

1. Neto, L.B.; Kotousov, A.; Bedrikovetsky, P. Elastic properties of porous media in the vicinity of the percolation limit. *J. Petrol. Sci. Eng.* **2011**, *78*, 328–333. [[CrossRef](#)]
2. Gajo, A.; Loret, B.; Hueckel, T. Electro-chemo-mechanical couplings in saturated porous media: Elastic-plastic behaviour of heteroionic expansive clays. *Int. J. Solids Struct.* **2002**, *39*, 4327–4362. [[CrossRef](#)]
3. Zhang, H.J.; Jeng, D.S.; Barry, D.A.; Seymour, B.R.; Li, L. Solute transport in nearly saturated porous media under landfill clay liners: A finite deformation approach. *Int. J. Solids Struct.* **2013**, *479*, 189–199. [[CrossRef](#)]
4. Wang, S.J.; Hsu, K.C. The application of the first-order second-moment method to analyze poroelastic problems in heterogeneous porous media. *Int. J. Solids Struct.* **2009**, *369*, 209–221. [[CrossRef](#)]
5. Mokni, N.; Olivella, S.; Li, X.L.; Smets, S.; Valcke, E. Deformation induced by dissolution of salts in porous media. *Phys. Chem. Earth* **2008**, *3*, S436–S443. [[CrossRef](#)]
6. Cao, N.; Lei, G. Stress sensitivity of tight reservoirs during pressure loading and unloading process. *Petrol. Explor. Dev.* **2019**, *46*, 1–7. [[CrossRef](#)]
7. Wang, W.D.; Shahvali, M.; Su, Y.L. A semi-analytical model for production from tight oil reservoirs with hydraulically fractured horizontal wells. *Fuel* **2015**, *158*, 612–618. [[CrossRef](#)]
8. Zhang, Q.; Su, Y.L.; Wang, W.D.; Lu, M.J.; Sheng, G.L. Gas transport behaviors in shale nanopores based on multiple mechanisms and macroscale modeling. *Int. J. Heat Mass Transf.* **2018**, *125*, 845–857. [[CrossRef](#)]

9. Zhang, Q.; Su, Y.L.; Wang, W.D.; Lu, M.J.; Sheng, G.L. Apparent permeability for liquid transport in nanopores of shale reservoirs: Coupling flow enhancement and near wall flow. *Int. J. Heat Mass Transf.* **2017**, *115*, 224–234. [[CrossRef](#)]
10. Zhang, C.; Yu, L.; Feng, R.M.; Zhang, Y.; Zhang, G.J. Numerical Study of Stress Distribution and Fracture Development above a Protective Coal Seam in Longwall Mining. *Processes* **2018**, *6*, 146. [[CrossRef](#)]
11. Jiang, H.J.; Yan, J.N. Experimental study on stress sensibility of fractured reservoir. *Spec. Oil Gas Reserv.* **2000**, *3*, 39–41. (In Chinese)
12. Fatt, I. Reduction in permeability with overburden pressure. *J. Petrol. Technol.* **1952**, *4*, 16. [[CrossRef](#)]
13. Buchsteiner, H.; Warpinski, N.R.; Economides, M.J. Stress-Induced Permeability Reduction in Fissured Reservoirs. In Proceedings of the SPE Annual Technical Conference and Exhibition, Houston, TX, USA, 3–6 October 1993. SPE26513-MS. [[CrossRef](#)]
14. Zhang, Y.; Cui, Y. Experimental study of pressure sensitivity on the gravel low permeability layer. *Oil Drill. Prod. Technol.* **1999**, *21*, 1–6. (In Chinese)
15. Jones, F.O.; Owens, W.W. A laboratory study of low-permeability gas sands. *J. Petrol. Technol.* **1980**, *32*, 1631–1640. [[CrossRef](#)]
16. Nelson, R.A. An experimental study of fracture permeability in porous rock. In Proceedings of the 17th US Symposium on Rock Mechanics, Snow Bird, UT, USA, 25–27 August 1976. ARMA-76-0127.
17. Archer, R.A. Impact of Stress Sensitive Permeability on Production Data Analysis. In Proceedings of the SPE Unconventional Reservoirs Conference, Keystone, CO, USA, 10–12 February 2008. SPE-114166-MS. [[CrossRef](#)]
18. Zimmerman, R.W.; Kumar, S.; Bodvarsson, G.S. Lubrication theory analysis of the permeability of rough-walled fractures. *Int. J. Rock Mech. Min.* **1991**, *28*, 325–331. [[CrossRef](#)]
19. Dobrynin, V.M. Effect of overburden pressure on some properties of sandstones. *Soc. Petrol. Eng.* **1962**, *4*, 360–366. [[CrossRef](#)]
20. Lan, L. Research on stress sensitivity and prediction of fracture width in naturally fractured sandstone reservoirs. Master's Thesis, Southwest Petroleum University, Chengdu, China, 2005. (In Chinese)
21. Gangi, A.F. Variation of whole and fractured porous rock permeability with confining pressure. *Int. J. Rock Mech. Min.* **1978**, *15*, 249–257. [[CrossRef](#)]
22. Li, D.Q.; Kang, Y.L.; Zhang, H. New evaluation method of permeability stress sensitivity based on visual fracture aperture measurement. *Nat. Gas Geosci.* **2011**, *2*, 494–500. (In Chinese)
23. Lei, G.; Dong, P.C.; Yang, S.; Wang, B.; Wu, Z.S. Study of stress sensitivity of low-permeability reservoir based on arrangement of particles. *Rock Soil Mech.* **2014**, *35*, 209–214. (In Chinese)
24. Advani, S.H.; Lee, T.S.; Avasthi, J.M. Parametric sensitivity investigations for hydraulic fracture configuration optimization: Rock Mechanics as a Guide for Efficient Utilization of Natural Resources. In Proceedings of the 30th U.S. Symposium, Morgantown, WV, USA, 19–22 June 1989. [[CrossRef](#)]
25. McKee, C.R.; Bumb, A.C.; Koenig, R.A. Stress-dependent permeability and porosity of coal and other geologic formations. *SPE Form. Eval.* **1988**, *3*, 81–91. [[CrossRef](#)]
26. David, C.; Wong, T.F.; Zhu, W.; Zhang, J. Laboratory measurement of compaction-induced permeability change in porous rocks: Implications for the generation and maintenance of pore pressure excess in the crust. *Pure Appl. Geophys.* **1994**, *143*, 425–456. [[CrossRef](#)]
27. Tong, S.Y.; Gu, M.; Singh, R.; Mohanty, K.K. Simulation of proppant transport in foam fracturing fluid based on experimental results. In Proceedings of the SPE/AAPG/SEG Unconventional Resources Technology Conference, Houston, TX, USA, 23–25 July 2018. URTEC-2901054-MS. [[CrossRef](#)]
28. Shrivastava, K.; Sharma, M.M. Proppant transport in complex fracture networks. In Proceedings of the SPE Hydraulic Fracturing Technology Conference and Exhibition, The Woodlands, TX, USA, 23–25 January 2018. SPE-189895-MS. [[CrossRef](#)]
29. Tong, S.Y.; Singh, R.; Mohanty, K.K. Proppant transport in fractures with foam-based fracturing fluids. In Proceedings of the SPE Annual Technical Conference and Exhibition, San Antonio, TX, USA, 9–11 October 2017. SPE-187376-MS. [[CrossRef](#)]
30. McClure, M.W.; Babazadeh, M.; Shiozawa, S.; Huang, J. Fully coupled hydromechanical simulation of hydraulic fracturing in 3D discrete-fracture networks. *SPE J.* **2016**. [[CrossRef](#)]
31. Wang, C.Y.; Du, X.Y. Experimental study on the splitting characteristics of sandstone in Brazil based on size effect. *Min. Res. Dev.* **2018**, *6*, 44–48. (In Chinese)

32. Peng, C.J.; Chen, C.C.; Xu, J.; Zhang, H.L.; Tang, Y.; Nie, W.; Zhao, K. Loading rate dependency of rock stress-strain curve based on Brazil splitting test. *J. Rock Mech. Eng.* **2018**, *A1*, 3247–3252. (In Chinese)
33. Zhan, Y.P.; Fu, C.L.; Li, S.Y. The artificial cracks preparation method for the tight sandstone fracture reservoir. *Res. Expl. Lab.* **2017**, *1*, 10–12. (In Chinese)
34. Li, C. Double effective stress of porous media. *Nat. Mag.* **1999**, *5*, 288–292. (In Chinese)
35. Qiao, L.P.; Wang, Z.C.; Li, S.C. Effective stress law for permeability of tight gas reservoir sandstone. *J. Rock Mech. Eng.* **2011**, *7*, 1422–1427. (In Chinese)
36. Duan, X.G.; An, W.G.; Hu, Z.M.; Gao, S.S.; Ye, L.Y.; Chang, J. Experimental study on fracture stress sensitivity of Silurian Longmaxi shale formation, Sichuan Basin. *Nat. Gas Geosci.* **2017**, *28*, 1416–1424. (In Chinese)
37. Ahammad, M.J.; Rahman, M.A.; Zheng, L.; Alam, J.M.; Butt, S.D. Numerical investigation of two-phase fluid flow in a perforation tunnel. *J. Nat. Gas. Sci. Eng.* **2017**, *55*, 606–611. [[CrossRef](#)]
38. Jiang, C.B.; Xu, Z.M.; Li, X.L. Fractional step finite element formulation for solving incompressible flows. *J. Tsinghua Univ. (Sci. Technol.)* **2002**, *42*, 278–280. (In Chinese)
39. Abdoukadi, C.; Stiaan, G.; Wang, R.J. Newton–Raphson Solver for Finite Element Methods Featuring Nonlinear Hysteresis Models. *IEEE. Trans. Magn.* **2018**, *54*, 1–8. [[CrossRef](#)]
40. Johari, A.; Heydari, A. Reliability analysis of seepage using an applicable procedure based on stochastic scaled boundary finite element method. *Eng. Anal. Bound. Elem.* **2018**, *94*, 44–59. [[CrossRef](#)]
41. Walsh, J.B. Effect of pore and confining pressure on fracture permeability. *Int. J. Rock Mech. Min.* **1981**, *18*, 429–435. [[CrossRef](#)]
42. Vahab, M.; Akhondzadeh, S.; Khoei, A.R.; Khalili, N. An X-FEM investigation of hydro-fracture evolution in naturally-layered domains. *Eng. Fract. Mech.* **2018**, *191*. [[CrossRef](#)]
43. Liu, X.D.; Morita, N. Collapse and bending analysis of slotted liners by 3D FEM under various reservoir Conditions. In Proceedings of the SPE Annual Technical Conference and Exhibition, Dallas, TX, USA, 24–26 September 2018. SPE-191441-MS. [[CrossRef](#)]
44. Tong, S.Y.; Mohanty, K.K. Proppant transport study in fractures with intersections. *Fuel* **2016**, *181*, 463–477. [[CrossRef](#)]
45. Wang, H.Y.; Sharma, M.M. Modeling of hydraulic fracture closure on proppants with proppant settling. *J. Petrol. Sci. Eng.* **2018**, *171*, 636–645. [[CrossRef](#)]
46. Tong, S.Y.; Singh, R.; Mohanty, K.K. A visualization study of proppant transport in foam fracturing fluids. *J. Nat. Gas Sci. Eng.* **2018**, *52*, 235–247. [[CrossRef](#)]
47. Zheng, J.T. Study on the stress-dependent properties of low-permeability rock and 3D rock porous structure reconstruction. Ph.D. Thesis, China University of Mining & Technology, Beijing, China, 2016.
48. Min, L.Y.; Lv, C.Y.; Zhang, B.W. SY/T6385—2016 Porosity and permeability measurement under overburden pressure. *Petrol. Indus. Press.* **2016**, *1*, 1–7. (In Chinese)

